

PAPER • OPEN ACCESS

Sub-nanosecond acousto-electric carrier redistribution dynamics and transport in polytypic GaAs nanowires

To cite this article: Maximilian M Sonner *et al* 2021 *Nanotechnology* **32** 505209

View the [article online](#) for updates and enhancements.

You may also like

- [Sound speed uncertainty in acousto-electric tomography](#)
Bjørn Christian Skov Jensen and Kim Knudsen
- [Acousto-electric transport in MgO/ZnO-covered graphene on SiC](#)
Y-T Liou, A Hernández-Mínguez, J Herfort et al.
- [Control of morphology and crystal purity of InP nanowires by variation of phosphine flux during selective area MOCVD](#)
A Kelrich, V G Dubrovskii, Y Calahorra et al.



IOP | ebooks™

Bringing together innovative digital publishing with leading authors from the global scientific community.

Start exploring the collection—download the first chapter of every title for free.

Sub-nanosecond acousto-electric carrier redistribution dynamics and transport in polytypic GaAs nanowires

Maximilian M Sonner¹ , Maximilian Gnedel¹, Johannes C Berlin¹, Daniel Rudolph², Gregor Koblmüller²  and Hubert J Krenner^{1,3} 

¹ Lehrstuhl für Experimentalphysik 1, Institut für Physik, Universität Augsburg, Universitätsstraße 1, D-86159 Augsburg, Germany

² Walter Schottky Institut and Physik Department, Technische Universität München, Am Coulombwall 4, D-85748 Garching, Germany

³ Physikalisches Institut, Universität Münster, Wilhelm-Klemm-Str. 10, D-48149 Münster, Germany

E-mail: krenner@uni-muenster.de

Received 28 July 2021, revised 16 September 2021

Accepted for publication 27 September 2021

Published 18 October 2021




CrossMark

Abstract

The authors report on a combined structural, optical and acousto-electric study of polytypic GaAs nanowires. Two types of nanowires with different zincblende and wurtzite crystal phase mixing are identified by transmission electron microscopy and photoluminescence spectroscopy. The nanowires exhibit characteristic recombination channels which are assigned to different types of spatially direct recombination (electron and hole within the same crystal phase segment) and spatially indirect recombination (electron and holes localized in different segments). Contact-free acousto-optoelectric spectroscopy is employed to resolve spatiotemporal charge carrier dynamics between different recombination channels induced by a piezoelectric surface acoustic wave. The observed suppression of the emission and its dynamic temporal modulation shows unambiguous fingerprints of the local bandedge variations induced by the crystal phase mixing. A nanowire, which exhibits a variation from a near-pristine zinc blende crystal structure to a highly mixed crystal phase, shows a clear dependence on the propagation direction of the acoustic wave. In contrast, no pronounced directionality is found for a nanowire with an extended near-pristine zincblende segment. The experimental findings are corroborated by solving the drift and diffusion equations of electrons and holes induced by the surface acoustic wave. The key characteristics observed in our experimental data are well reproduced in the numerical simulations by assuming two general bandedge modulations and realistic parameters for the bandedge discontinuities and transport mobilities of electrons and holes. This evidences that even all relevant physical processes are accounted for in the model.

Supplementary material for this article is available [online](#)

Keywords: acoustoelectric effect, polytypism, surface acoustic waves, nanowire

 Original content from this work may be used under the terms of the [Creative Commons Attribution 4.0 licence](#). Any further distribution of this work must maintain attribution to the author(s) and the title of the work, journal citation and DOI.

1. Introduction

Semiconductor nanowires (NWs) are heavily investigated semiconductor nanoscale structures and are considered as extremely promising candidates for future high performance nanoelectronic and nanophotonic devices [1–5]. However, in such semiconductor NWs, the mixing of zinc blende (ZB) and wurtzite (WZ) crystal phases occurs frequently along the NW

axis and leads to a static type-II modulation of the conduction (CB) and valence band (VB) edges [6–11]. This results in a carrier localization within different regions and in the opening of new channels, e.g. for optical recombination and electrical transport. Thus, a free exciton transition in the pure ZB phase and two bound, indirect exciton transitions at ZB twinning defects and at the interface of WZ and ZB segments, respectively, were observed [12–20]. In addition to the optical properties, stacking fault defects and crystal phase boundaries acting as scattering centers certainly affect carrier transport along the NWs [21–24]. Hence, the understanding of charge carrier dynamics and the interaction of different, interconnected channels in such NWs is essential for optimization of such devices.

Surface acoustic waves (SAWs) are routinely employed to sense and manipulate on the nanoscale due to their universal coupling to literally any type of system [25]. When these waves [26] propagate on a piezoelectric chip, strain induces an electric field [27]. This electric field can be employed as a versatile conductivity probe [28–34]. Moreover, this electric field, in turn, efficiently ionizes weakly bound excitons [35, 36] and induces spatiotemporal dynamics of such dissociated electrons and holes in semiconductor nanostructures [37]. The induced dynamics strongly modulate the optical emission in the time domain and their characteristic fingerprints can be detected in photoluminescence (PL) experiments [24, 37–41]. This so-called acousto-optoelectric spectroscopy (AOES) provides direct insights of the charge carrier dynamics in such nanoscale semiconductor structures, utilizing the acoustoelectric coupling between charge carriers and the SAW's piezoelectric field [35, 41–45].

Recently, these acousto-optoelectric experiments have been performed on various semiconductor NW heterostructures by transferring such NW structures onto piezoelectric LiNbO₃ SAW chips. With this technique, the underlying spatio-temporal carrier dynamics induced by the SAW are investigated by the temporal modulation of the optical emission [46]. Thus, charge carriers are transported along a NW and injected into quantum dots and defects for triggered photon emission by the remote carrier control via SAWs on a sub-nanosecond timescale [45, 47, 48]. Moreover, this contact-free AOES allows to derive the transport mobilities of electrons and holes, as well as to study the impact of local potential modulations of individual GaAs/AlGaAs core/shell and halide perovskite NWs in the fundamental, native material limit of low carrier density by comparing experiment and numerical modeling of the charge carrier dynamics [24, 40].

Here, we report on an AOES study conducted on two different types of polytypic GaAs-AlGaAs core-shell nanowires demonstrating charge carrier transfer between different transition channels occurring in each type of NW. NWs of the first type show variation of the crystal structure along the NWs from near-pristine NWs of ZB phase with a low twin defect density, to highly polytypic NWs with extended WZ segments embedded in an otherwise ZB phase. In contrast, the crystal structure of the second type of NWs is pure ZB with the twin defect density slightly increasing along the NW

(with no WZ segments). Finally, we resolve the resulting SAW-driven spatio-temporal carrier dynamics in the temporal modulation of each transition channel by corroborating our experiments with numerical simulations that model the carrier dynamics.

The results are presented in the following section 2 which is structured as follows: section 2.1 presents results of structural and optical characterization of exemplary NWs. The two NWs selected for optical experiments are studied by AOES in section 2.2. The AOES setup is introduced in 2.2.1 and experimental results of time-integrated and time-resolved AOES are presented in 2.2.2 and 2.2.3, respectively. In 2.2.3, the experimental data are compared to numerical simulation of the SAW-driven spatio-temporal carrier dynamics for exemplary bandedge modulations for the two types of NWs found in our structural characterization. These simulations nicely reproduce key features of the experimental data, demonstrating that the two assumed simple geometries are sufficient to gain insight into the underlying processes. The main findings of this paper are summarized and discussed in section 3.

2. Results

2.1. Structural and optical characterization

NWs were grown on a Si (111) substrate in a solid-source molecular beam epitaxy system by a Ga-assisted autocatalytic growth process [49, 50]. The as-grown structure nominally consists of a GaAs core with a diameter of 60–80 nm and typical lengths $l_{NW} > 10 \mu\text{m}$, which is overgrown by a 60 nm thick Al_{0.3}Ga_{0.7}As shell [49] to suppress non-radiative surface recombination of carriers [51]. Additionally, a 3 nm thick radial GaAs quantum well (QW) is embedded in the center of the shell [52]. This QW is effectively decoupled from the GaAs core by the thick barrier [45] and not considered further in this paper. For passivation, a GaAs capping layer of 10 nm was added to prevent the oxidation.

To determine the microstructural properties along the axis of such grown NWs, we performed high-resolution transmission electron microscopy (TEM) on representative NWs. Figures 1(a) and (b) show TEM images of two representative NWs acquired along their entire length. Additional TEM analysis of the representative Type-1 NW is included in the supporting materials (available online at stacks.iop.org/NANO/32/505209/mmedia) in supporting section 1. In addition, selected diffraction patterns are taken in the upper and lower part of both NWs. Both types of NWs differ in the variation of their crystal structure along the NW axis. NWs, referred to as Type-1 (figure 1(a)), consist in the lower part of a ZB crystal structure with occasional rotational twins separated by individual twin defects, as confirmed by the associated diffraction pattern. In this region the diffraction pattern clearly shows the characteristic ZB reflections of individual ZB twin defects (ZB-A and ZB-B sensitive reflections are marked by red and blue circles). Such twin defects can be understood as a monolayer thick insertion of the WZ material

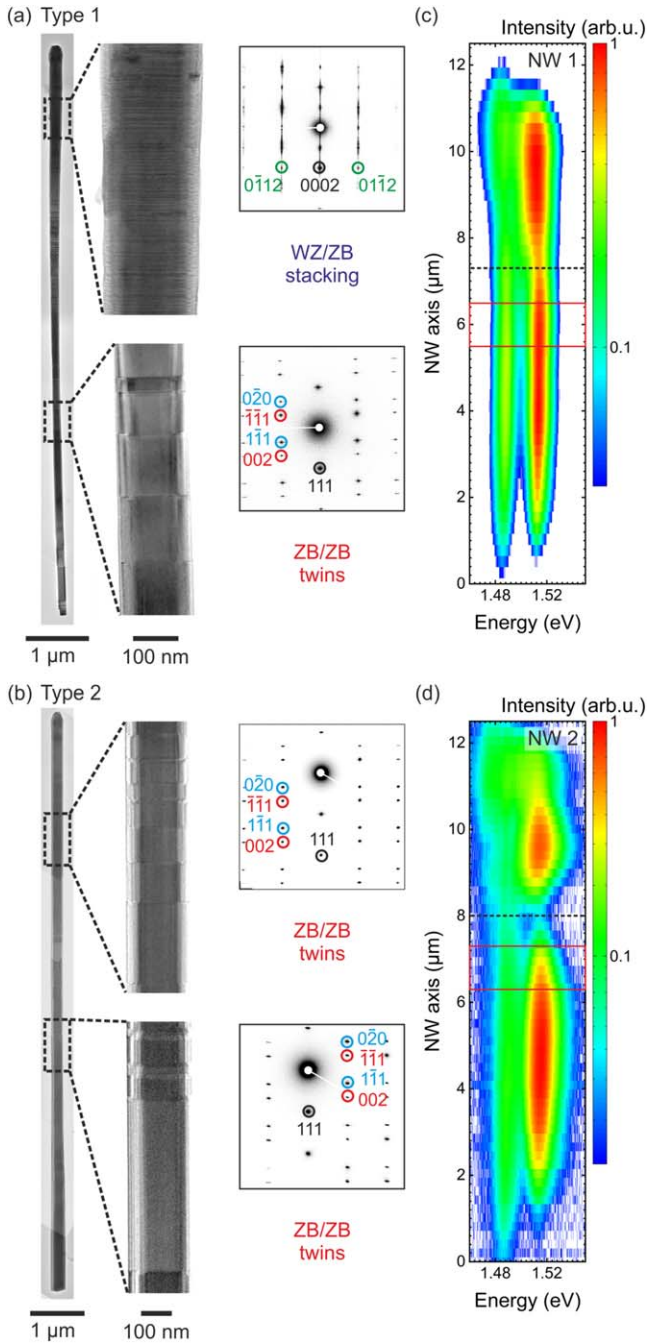


Figure 1. (a), (b) TEM images and corresponding diffraction patterns of two different GaAs-AlGaAs core-shell NWs. (a) The lower region of Type-1 NW exhibits a ZB crystal structure with few twin defects. ZB-A and ZB-B sensitive reflections are marked by blue and red circles. The upper region contains also larger WZ phase segments and defects. WZ sensitive reflections, as marked by green circles, are clearly visible in the diffraction pattern. (b) NW of Type-2 exhibits a ZB crystal structure along the entire NW with the twin defect density slightly increasing towards the upper end. (c), (d) Spatial PL maps along two further NWs, referred to as (c) **NW1** and (d) **NW2** at low optical pump power densities ($2.8 - 8.5 \text{ W cm}^{-2}$). **NW1** and **NW2** are associated with a crystal structure of Type-1 and Type-2, respectively. The black dashed lines mark the change of the crystal structure along the NWs. The red boxes indicate the region of excitation along the NW for AOEES.

in a ZB matrix [19, 20, 53, 54]. Towards the upper part of the NW the crystal structure becomes more disordered with a higher density of rotational twin defects. At the top of the NW, it exhibits a larger number of extended WZ segments within the ZB phase. Consequently, the diffraction pattern in the upper part exhibits characteristic WZ reflections (marked by green circles) and streaks confirming the high disorder in the crystal structure. In contrast, NWs referred to as Type-2 (figure 1(b)), only exhibit ZB phase domains along the NW and no extended WZ segments occur. In addition, the density of rotational twin defects increases only slightly towards the upper part and results in a larger number of short ZB segments, yet no WZ segments occur. Hence, both diffraction patterns, at the lower and at the upper region of the NW, exhibit exclusively ZB reflections. Consequently, NWs of Type-2 can be considered as more homogenous along the axis compared to NWs of Type-1. These changes of crystal structure have a pronounced impact on the optical properties of NWs, which we confirm by optical spectroscopy.

Figures 1(c) and (d) show low temperature ($T = 8 \text{ K}$) microphotoluminescence ($\mu\text{-PL}$) spectral maps along the axis of two representative NWs, which we refer to as **NW1** and **NW2**, respectively. Details on the experimental setup and parameters are included as supporting section 2 in the supporting materials of this paper. The color-coded emission intensity is plotted in logarithmic scale as a function of the axial position and photon energy. Moreover, we included the same data plotted in linear scale in SFigure SF2 of supporting section 3 to clearly visualize the peak shifts. Both NWs show characteristic, position-dependent changes of their emission spectra along their axes and exhibit a pronounced reduction of the emission intensity at approximately the same position along their axis marked by black dotted lines. This observation points towards a change of the microstructure during growth of the NW core. In the following, we analyze the spectra of both NWs in the regions marked by red boxes. In these regions, we also conducted AOEES to assess the impact of polytypism on the spatio-temporal carrier dynamics.

In the two types of NWs, we can readily distinguish different recombination channels characteristic for polytypic GaAs NWs. We introduce these different possible recombination channels in figures 2(a) and (b). Our assignments are fully consistent with previous works, in particular references [54, 55]. They can be identified in the measured PL spectra recorded near the center of **NW1** and **NW2** shown in figures 2(c) and (d), respectively. Additional data such as fitting results of all three peaks and the corresponding time transients are included in the supporting materials in SFigure SF3 in supporting section 3. In the spectra of both NWs, the emission of direct excitons in the pure ZB phase (blue boxes in figures 2(a) and (b)) is detected at a photon energy $E_{\text{ZB}} = 1.514 \text{ eV}$, which is marked by blue arrows. At lower photon energies, both spectra of both NWs exhibit another common emission peak at $E_{\text{ZB}/\text{twin}} = 1.488 \text{ eV}$, marked by green arrows in figures 2(c) and (d). This emission signal is

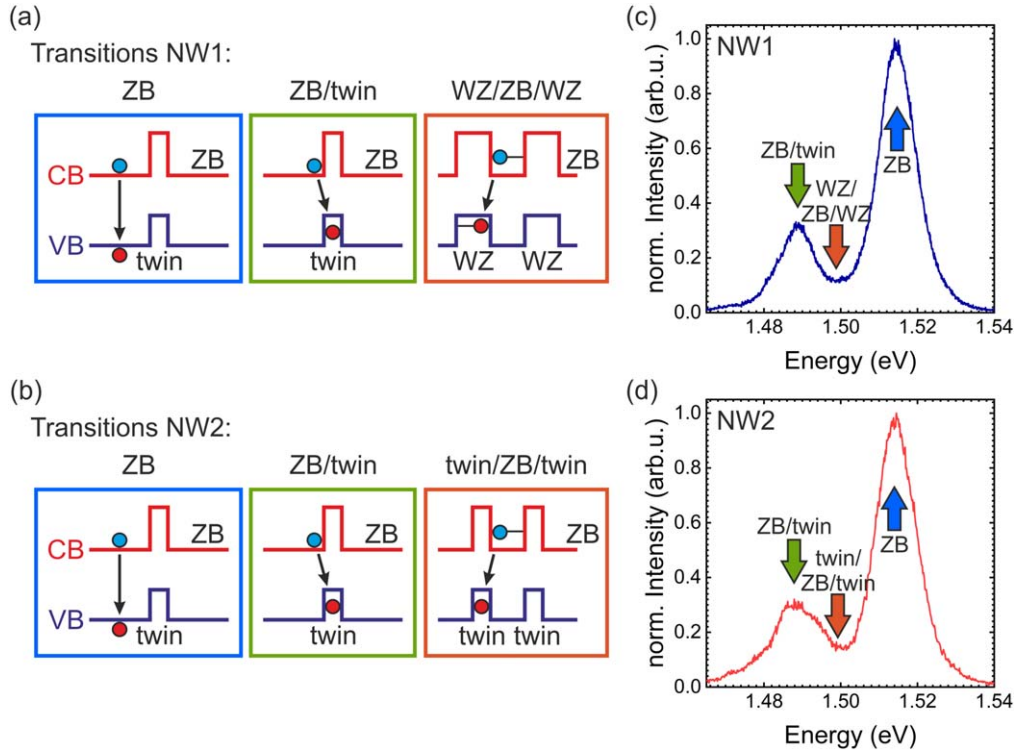


Figure 2. (a), (b) Schematics of the emission processes occurring in each NWs. Recombination of direct excitons in pure ZB phase (ZB) and spatially indirect excitons localized at twin defects (ZB/twin) exists in both NWs. In **NW1**, indirect exciton recombination occurs between quantum confined electrons in short ZB segments and quantum confined holes in short WZ-segments (WZ/ZB/WZ), whereas indirect excitons are present between quantum confined electrons and holes localized at twin defects (twin/ZB/twin) in **NW2**. (c), (d) Typical photoluminescence spectra observed at the center of **NW1** and **NW2**, respectively. Arrows mark the different recombination transitions.

referred to ZB/twin transitions (green boxes in figures 2(a) and (b)) and results from the recombination of quasi-free electrons in extended ZB phase regions and quantum confined holes at rotational twin defects [54]. The corresponding emission is observed at lower energy. The position-dependent PL-data of **NW1** in figure 1(c) shows that the main ZB emission peak slightly shifts toward lower energies and broadens in the upper part of the NW compared to the lower part. This effect is directly linked to the change in the crystal structure. The shifted signal is attributed to the indirect exciton transitions at the interface of short WZ and ZB segments in the highly mixed region of **NW1** (referred as WZ/ZB/WZ recombination) shown schematically in the orange box figure 2(a). This WZ/ZB/WZ recombination occurs between quantum confined electrons in short ZB segments and quantum confined holes in short WZ-segments in the highly mixed region of **NW1**, leading to the observed shift of the emission energy [54]. In the spectrum of figure 2(c) these are marked by the orange arrow. In contrast, **NW2** exhibits no shift in energy of the ZB emission peak. Thus, the emission between that of the ZB- and ZB/twin channels is attributed to indirect exciton transitions between quantum confined electrons and holes localized at twin defects (referred to as twin/ZB/twin recombination) and is marked by the orange arrow in figure 2(d). As for the WZ/ZB/WZ and twin/ZB/twin recombination, both types of charge carriers are confined, which results in a shift to higher (lower) energies compared to the ZB/twin (ZB) emission peak.

2.2. Acousto-optoelectric spectroscopy

After characterizing the unperturbed NW emission, we study the charge carrier dynamics by AOES at the position along the NW axis showing the corresponding PL spectra depicted in figures 2(c), (d), respectively. We have shown that the degree of polytypism varies along the NW axis, hence we expect that the propagation direction of the driving SAW has a pronounced impact on the resulting charge carrier dynamics.

2.2.1. AOES setup. For our AOES measurements, we transfer GaAs/AlGaAs core/shell NWs onto a YZ-cut LiNbO₃ substrate with lithographically patterned interdigital transducers (IDTs) as shown schematically in figure 3(a). The SAW-chip is equipped with two nominally identical IDTs, which allows the generation of two SAWs that propagate in opposite directions. These two directions are referred to as $+k$ (left to right, red arrow) and $-k$ (right to left, blue arrow) propagating SAWs. These IDTs are used to generate SAWs with a wavelength of $\lambda_{SAW} = 18 \mu\text{m}$ by applying a resonant radio frequency (RF) signal. The corresponding acoustic period and SAW frequency are $T_{SAW} = 5.08\text{ns}$ and $f_{SAW} = 197 \text{MHz}$, respectively. For our experiments, we selected NWs aligned parallel to the propagation of the SAW and studied their optical emission by AOES. Crucial for AOES is that charge carriers can be photogenerated at a well-defined local phase of the SAW by actively referencing the RF signal to the repetition frequency of the laser, $n \cdot f_{Laser} = f_{SAW}$, with n being integer [24, 45, 46, 56, 57]. As the SAW

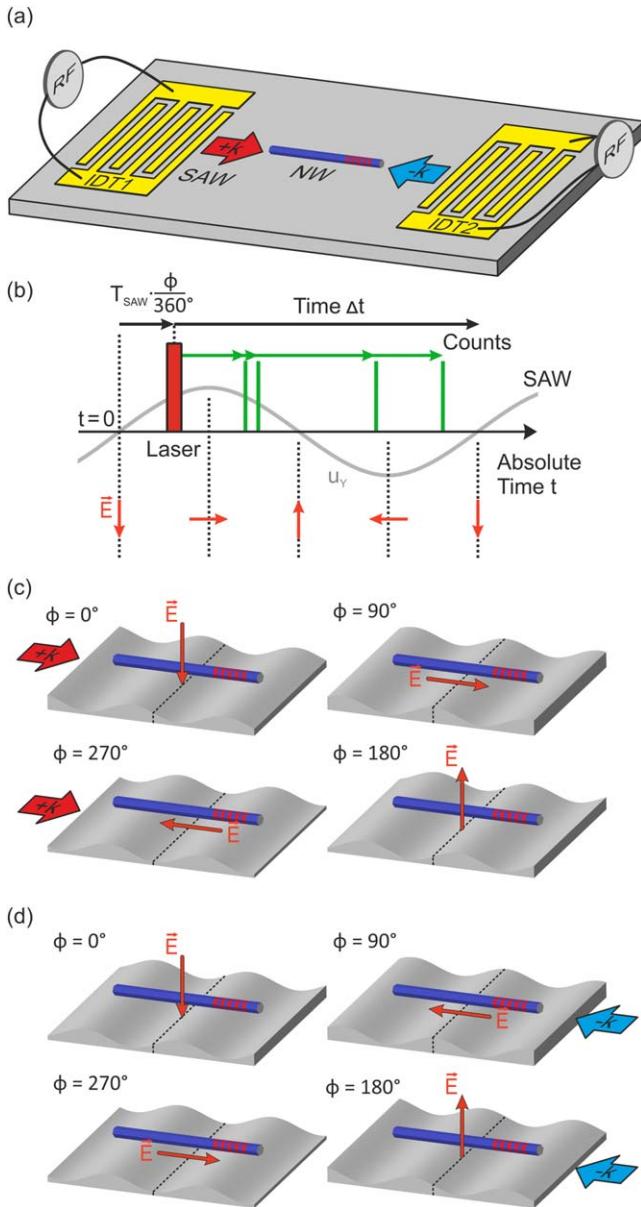


Figure 3 (a) Schematic of a typical SAW device consisting of two IDTs to generate $+k$ and $-k$ propagating SAWs (not to scale). NWs used for AOES are aligned parallel to the propagation direction of both SAWs. (b) Timing scheme of the AOES experiment. The absolute time, t , of the experiment is set by local phase of the SAW oscillation (grey, u_y , vertical displacement). Electrons and holes are injected by photoexcitation using a pulsed laser (red bar) at different SAW phases which are delayed by $T_{SAW} \cdot \phi / 360^\circ$. The individual time stamps of subsequent detection events are detected relative to the laser excitation. (c), (d) Schematics of relative orientation of a NW and the components of the SAW-induced electric field at a fixed point relative to the SAW and different SAW phases ϕ between laser and SAW excitation for (c) $+k$ and (d) $-k$ propagating SAWs. Electric field periodically gyrates at a fixed position (laser spot) along the NW with time.

propagates, the electric field vector gyrates counterclockwise close to the surface of the LiNbO_3 substrate used in this work. This leads to an acceleration of the electrons along the NW. We collect and spectrally disperse the emission of the NW. Signal

components of different emission bands are analyzed either by time-integrated multi-channel detection using a cooled CCD detector or after spectral filtering in the time-domain by single photon detectors and time-correlated single photon counting. The full timing scheme of the experiment is presented in figure 3(b). The absolute time, t , is set by the SAW at the position of the laser spot on the NWs. As the absolute time, t , progresses, the electric field vector gyrates counterclockwise. Moreover, by setting the phase ϕ between the laser and the SAW excitation from 0 to 360° , charge carriers can be generated at a well-defined phase of the SAW cycle which can be delayed by $T_{SAW} \cdot \phi / 360^\circ$. In figures 3(c) and (d), schematics of the relative orientation of NW and the oscillating components of the SAW-induced electric field [27] is shown at fixed SAW phases for $+k$ - and $-k$ -propagating SAW defining the orientation of the electric field and NW axis. For instance, at one distinct phase during the SAW oscillation, the electric field component is pointing perpendicular to the surface towards the substrate. We use this excitation condition as our reference for the experiments and define the corresponding SAW phase of $\phi = 0^\circ$ between laser excitation and SAW oscillation. In turn, the electric fields at $\phi = 90^\circ$ and 270° are aligned parallel and antiparallel to SAW propagation direction. Finally, the individual time stamps of subsequent detection events are detected relative to the laser excitation [24, 58].

2.2.2. Time-integrated spectroscopy. In figures 4(a), (b), we present the time-integrated PL emission spectra of both NWs as a function of the applied RF power (P_{RF}) for $+k$ - (left panels) and $-k$ - (right panels) propagating SAWs. Both NWs are aligned the same way, which is shown by the schematics on the top. Hence, the $+k$ - and $-k$ -directions point towards and away from the highly polytypic regions, respectively. As P_{RF} and, thus, the SAW's electric field amplitude increases, the overall PL emission is quenched due to the separation of electrons and holes. Apparently, the quenching behavior of the ZB and ZB/twin emissions clearly differs for the NW1 (figure 4(a)) when the propagation direction of the SAW is reversed, while no marked difference is present for NW2 (figure 4(b)). Moreover, we find that the emission of the ZB/twin excitons of NW1 is shifted towards higher energies for both propagation directions, whereas the indirect exciton energy of NW2 is not affected by the SAW. We further analyze this quenching behavior by extracting the normalized integrated PL intensity of all three emission bands from these spectra (normalized to the unperturbed emission, $P_{RF} < -28$ dBm). The obtained data are plotted in figures 4(c), (d) for the direct exciton transition in ZB GaAs (blue) and the indirect ZB/twin exciton transition at twin defects (green) and the indirect exciton transition between confined electrons and confined holes (orange), respectively. Considering each transition individually, the ZB transition and the ZB/twin transition show a similar, continuous quenching behavior for both NWs and for the SAW propagation in reversed directions. These observations are similar to that known for other III-V semiconductor nanosystems [24, 35, 36, 40, 46]. Note, the non-monotonic quenching of the PL intensity of the ZB emission, i.e. the weak increase of

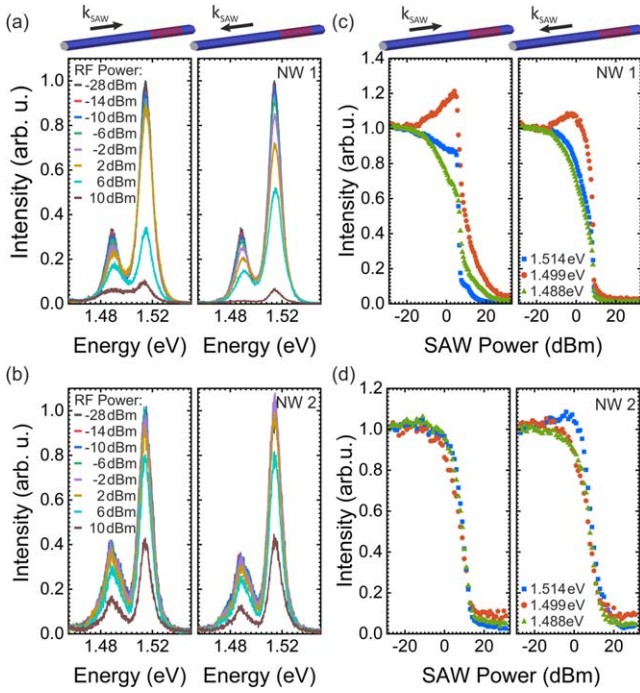


Figure 4. (a), (b) Emission spectra at the center of (a) NW1 and (b) NW2 modulated by a SAW at a frequency $f_{SAW} = 197$ MHz for varying SAW intensity P_{RF} applied at the IDTs and $+k$ -propagating (left panels) $-k$ -propagating (right panels) SAW. With increasing SAW power density, the overall emission is quenched due to the efficient dissociation and acceleration of electrons and holes by the piezoelectric field of the SAW. (c), (d) Extracted normalized PL intensities of the free excitons in pure ZB crystal phase at 1.515 eV and the indirect excitons transitions at twin defects at 1.488 eV, and indirect excitons between confined electrons and confined holes at 1.499 eV of (c) NW1 and (d) NW2 as a function of SAW power P_f .

the overall intensity at low acoustic powers, is well known in literature for 1D and 2D systems [38, 47]. It arises from an increase of the electron–hole overlap due to their dissimilar carrier mobilities [38]. In contrast, the evolution of the integrated intensity of the indirect WZ/ZB/WZ exciton transitions (orange) of **NW1** (figure 4(c)) is different compared to the indirect twin/ZB/twin exciton transitions of **NW2** (figure 4(d)). Most strikingly, for **NW1**, the PL intensity is not decreasing monotonically. The intensity reaches a pronounced maximum at low acoustic power levels (0 ± 4 dBm) and then decreases until it is almost fully suppressed. Such non-monotonic quenching has been previously observed for systems with zero-dimensional trapping sites or quantum dots [59, 60]. Thus, our observation suggests either an injection of charge carriers into the highly mixed WZ/ZB region leading to the formation of indirect excitons [60] or a suppression of a depletion of these excitons from this region [59], and is expected to occur in NWs of Type-1. In contrast, **NW2** exhibits a monotonous suppression of the PL emission band between the ZB- and ZB/twin channels. Hence, the feeding of higher energetic indirect transition channels, such as the WZ/ZB/WZ transition is expected to be absent and, thus, is more likely to occur in NWs of Type-2. Moreover, such a

behavior can be attributed to a more homogeneous distribution of trapping sites along the NW axis compared to **NW1**.

2.2.3. Time-domain spectroscopy. Next, we study the impact of the band edge modulation induced by polytypism on the acoustically driven carrier dynamics for **NW1** and **NW2**. To gain a deeper understanding of the underlying mechanisms, we analyze the dynamic modulation of the three characteristic emission bands at SAW powers of $P_{RF} = 7 \pm 3$ dBm and compare these experimental findings to numerical calculations of the SAW-driven carrier dynamics for model band edge modulations for both SAW propagation directions. In the following we restrict ourselves to one SAW-propagation direction, a $+k$ -propagating SAW to highlight our key findings. Fully detailed data and their comprehensive analysis for both $+k$ - and $-k$ -propagating SAWs can be found in supporting section 4 of the supporting materials.

In figures 5(a) and 6(a), we plot the PL time transients of all three transitions of **NW1** and each of **NW2** for selected SAW phases ϕ and $+k$ -propagating SAWs as a function of the absolute time $t = T_{SAW} \cdot \phi/360^\circ + \Delta t$. All three transitions of both NWs show characteristic and T_{SAW} -periodic intensity modulations. These modulations are not in phase but exhibit clear correlations and anti-correlations, which point towards coupled charge carrier dynamics. Furthermore, the recorded transients depend on the SAW phase ϕ , which nicely demonstrates that the orientation of electric field at the position of the laser spot at the time of the laser excitation programs subsequent SAW-driven carrier dynamics [24, 39]. Finally, also the SAW propagation direction has a pronounced impact on the observed intensity modulations.

To gain detailed understanding and obtain quantitative information on the charge carrier dynamics and the emission properties along the NW, we calculated the SAW-induced spatiotemporal carrier dynamics using a one-dimensional model. In essence, we calculate the spatio-temporal dynamics of the electron (n) and hole (p) concentration by solving the semiclassical drift and diffusion equations for a band edge modulation set by the electric potential of the SAW and the static bandedge modulation induced by the polytypic crystal structure. For full details of the model we refer to references [24, 37, 38]. Furthermore, we evaluate the product $n \cdot p$ which is proportional to the optical recombination intensity observed in our experiment. The results for the two basic geometries for NWs of Type-1 (**NW1**) and Type-2 (**NW2**) are shown for $+k$ -propagating SAWs in figures 5(b) and 6(b), respectively. For these calculations, we assume a basic geometry of a static type-II band modulation of an otherwise pure ZB NW with separated embedded WZ-type and twin-type segments. The band edge modulations of these geometries, which are basic versions of Type-1 and Type-2 NWs found in our TEM analysis (see figure 1), are shown schematically in the right panels, respectively. For both geometries we introduce a single twin-type segment with effective band offsets $\Delta E_{C,1}$ and $\Delta E_{V,1}$ (in the CB and VB) in

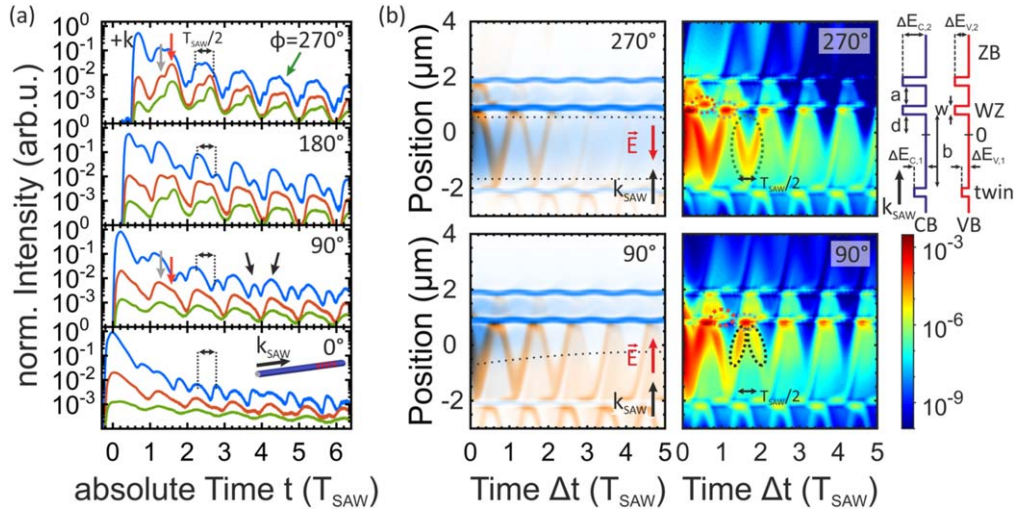


Figure 5. (a) Time-resolved PL emission spectra of the free ZB (blue), the indirect ZB/twin (green) and indirect WZ/ZB/WZ (orange) exciton transitions of NW1 for $+k$ -propagating SAW and different SAW phases ϕ . Note that data are plotted as function of absolute time t and therefore, changing ϕ leads to the observed delay of the onset of the transients. Traces are offset vertically for clarity. (b) Calculated electron (orange) and hole (blue) dynamics (left panels) and the product of electron and hole distribution (center panels) as a function of time and position for $+k$ -propagating SAW at SAW phases $\phi = 90^\circ$ and 270° . Charge carrier generation occurs at $x = 0$. Black dotted lines, as a guide to the eye in the left panels indicate the hole distribution in the ZB part of the NW. Right panels: Schematic of the corresponding band edge modulation of two separate WZ segments within a ZB NW for both SAW propagation directions. Black and green dotted ellipses in center panels of (b) highlight the change of the intensity modulation of the free ZB transition (marked by black and green arrows). Red and grey dotted ellipses in (b) indicate the distinct features of indirect transients marked by corresponding arrows in (a).

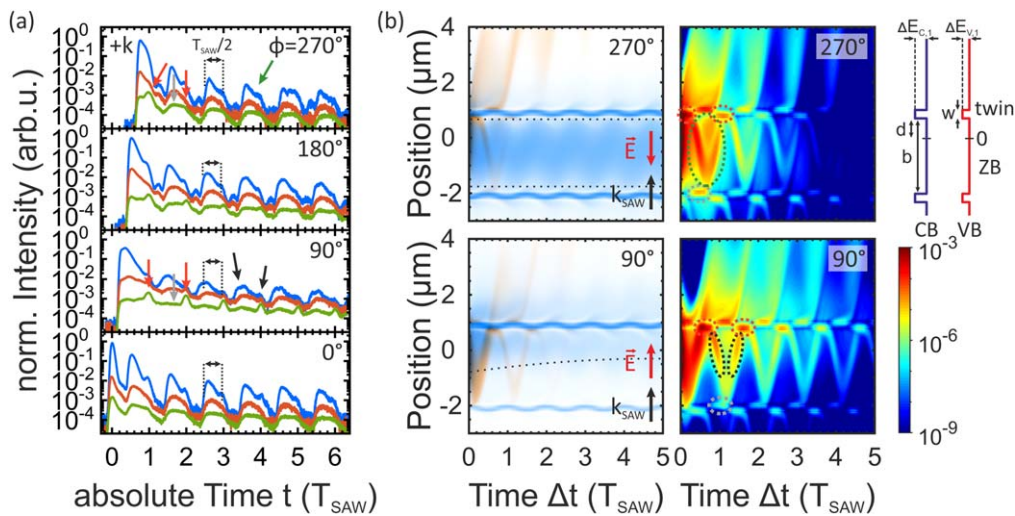


Figure 6. (a) Time-resolved PL emission spectra of the free ZB (blue), the indirect ZB/twin (green) and indirect twin/ZB/twin (orange) exciton transitions of NW 2 for $+k$ -propagating SAW and different phases ϕ . Traces are offset vertically for clarity. (b) Calculated electron (orange) and hole (blue) dynamics (left panels) and the product of electron and hole distribution (center panels) as a function of time and position for $+k$ -propagating SAW. Charge carrier generation occurs at $x = 0$. Black dotted lines, as a guide to the eye in the left panels indicate the hole distribution in the ZB of the NW. Right panels: Schematic of the corresponding band edge modulation of two twin defects within a ZB NW for both SAW propagation directions. Black and green dotted ellipses in center panels of (b) highlight the change of the intensity modulation of the free ZB transition (marked by black and green arrows). Red and grey dotted lines in (b) indicate the distinct features of indirect transients marked by corresponding arrows in (a).

the lower part of each NW representing the low rotational twin density in the lower parts of both types of NWs. In the upper parts, both NWs differ from each other in their band modulation. Most crucial, a Type-1 NW consists of two separated WZ-type segments in the upper part of the NW. In addition, the effective band offsets of these WZ-type segments were set to $\Delta E_{C,2}$ and $\Delta E_{V,2}$ in the CB and VB, respectively, being twice the effective band offset for the

segment in the lower part. For a Type-2 NW, there is only one second twin-type barrier with effective band offsets $\Delta E_{C,1}$ and $\Delta E_{V,1}$ in the upper part of the band structure. Both models predominantly reflect the highly disordered upper part of Type-1 NWs and the more homogeneous crystal structure with rotational twins along the axis of Type-2 NWs. Note, all segments have a width of $w = 200$ nm. Moreover, the twin segment in lower part of the NW and the first WZ segment of

Table 1. Dimensions of the static type-II band modulation along **NW1** and **NW2** as shown in the right panels of figures 5(b) and 6(b). Both geometries are based on TEM analysis. **NW1** represents NWs of Type-1, whereas **NW2** is associated with Type-2. Here, w is the width of each segment. In addition, b and a are the separation of the twin segment in lower part and the first WZ segment of the upper part as well as the separation of the WZ-type segments in the upper part, respectively. d is the distance of the nearest segment to the generation spot. ΔE_C and ΔE_V are the corresponding effective band offsets in the CB and VB.

$\Delta E_{C,1}$	$\Delta E_{V,1}$	$\Delta E_{C,2}$	$\Delta E_{V,2}$	w	b	d	a
7.5 meV	5.5 meV	15 meV	11 meV	200 nm	2.8 μm	800 nm	800 nm

the upper part are separated by a distance of b , while we chose a small distance a between the two WZ segments in the upper part of a Type-1 NW. In addition, the nearest segment is in a distance d to the generation spot at the center (position $x = 0$). The values used in the two simulations are summarized in table 1. Furthermore, electron hole pairs in both models are generated in between the twin-type segment in the lower part and the segments in the upper part. The mobility of electrons and holes were set to $\mu_n = 500 \text{ cm}^2 \text{ V}^{-1} \text{ s}^{-1}$ and $\mu_p = 50 \text{ cm}^2 \text{ V}^{-1} \text{ s}^{-1}$, respectively [24]. Note, $\mu_p = 0.1\mu_n$ implies that holes remain quasi-stationary at the time of photoexcitation for the range of parameters considered in our simulations. In figures 5(b) and 6(b) and, we plot the calculated electron (n , blue) and hole (p , orange) trajectories (left panels) and their product ($n \cdot p$, center panels) for a Type-1 and Type-2 NW as a function of time Δt (horizontal axis) and position x (vertical axis) for $+k$ -propagating SAWs, respectively. As noted before, the calculated trajectories show the spatio-temporal dynamics of each carrier species, and $n \cdot p$ can be related to the optical recombination intensity observed in the experiment. The upper and lower panels show results for delays $\phi = 90^\circ$ (electric field parallel to SAW propagation) and $\phi = 270^\circ$ (electric field antiparallel to SAW propagation), respectively.

We begin our evaluation of the acoustically driven dynamics of **NW1**. Data of the three transitions (ZB: blue, ZB/twin: green, WZ/ZB/WZ: orange) are presented for different SAW phases at the time of photoexcitation ϕ and the $+k$ -propagation in figure 5(a). Clearly, all transients show the expected characteristic modulations which are induced by the SAW. These modulations strongly depend on the studied recombination channel and the direction of the SAW.

For the SAW phase $\phi = 0^\circ$ (lower panel), the ZB exciton transition (blue transient) exhibits in experiment a $T_{\text{SAW}}/2$ -periodic intensity modulation. As ϕ is tuned from the lower to the upper panel, the temporal delay of the two recombination events increases first and becomes maximum at $\phi = 90^\circ$. Afterwards the delay decreases, exhibiting again a $T_{\text{SAW}}/2$ -periodic intensity oscillation at $\phi = 180^\circ$ and finally one broad T_{SAW} -periodic intensity modulation at $\phi = 270^\circ$. In contrast, the indirect ZB/twin transition at single twin defects at 1.488 eV (green transient) shows a T_{SAW} -periodic intensity modulation consisting of two major recombination events marked by grey and red arrows in figure 5(a). Again, these transients clearly depend on the SAW phase ϕ . After the initial decay at photoexcitation, the emission of the indirect ZB/twin transition reemerges at $t = 5T_{\text{SAW}}/4$ (grey arrow) for all SAW phases and becomes more pronounced as the phase is

tuned from $\phi = 0^\circ$ to 270° . The second recombination event occurs at $t = 8.3 \text{ ns}$ (red arrow) and is reduced in the intensity compared to the first event for $\phi = 0^\circ$ and 90° . Tuning the SAW phase from $\phi = 0^\circ$ to 270° results in the increase of emission intensity at $t = 8.3 \text{ ns}$ which exceeds the emission intensity of the first event for the SAW phases $\phi = 180^\circ$ and 270° . Moreover, this increased emission intensity at $t = 8.3 \text{ ns}$ gradually decreases compared to the first event with each SAW period until a steady state is reached at which both features have approximately the same intensity. The emission of WZ/ZB/WZ transition (orange) shows a time-modulation as the ZB/twin transition (green) which is expected as both are spatially indirect transitions. The observed subtle differences may be associated with electron confinement in the short ZB segments within mixed WZ/ZB/WZ region leading to electron levels at higher energies in the ZB phase of the stacking fault. Consequently, such weakly bound electrons would result in slightly different electron dynamics as electron activation from the stacking faults might be increased.

Key characteristics of the modulation of the transients are well reproduced by our numerical modeling: in figure 5(b), we show data for electric field along the NW being orientated parallel and antiparallel to the SAW propagation direction ($\phi = 90^\circ$ and $\phi = 270^\circ$). We begin by analyzing the spatio-temporal dynamics of the two carrier species. These are plotted in false-color representation [n (orange), p (blue)] as a function of Δt (horizontal axis) and position (vertical axis). For both SAW phases our simulations show that holes (blue) are mostly localized inside the two WZ segments of the upper part of the NW and in the center ZB part of the NW. In addition, few holes can be also found in the lower twin segment. Electrons (orange) are found in between the two WZ segments and in the overall lower ZB part. As time progresses, electrons and holes show sinusoidal trajectories driven by the electric field of the SAW, which are smeared out in space and time for holes due to their lower mobility. Furthermore, most electrons in the lower ZB part of the NW are periodically accelerated towards the first upper WZ segment from which they are mainly reflected. As a fraction of the electrons can overcome these barriers, they can be transferred into the region between the two upper WZ-segments. In addition, electrons are also either reflected by the lower twin segment or can overcome this CB barrier. Similar to our experimental data, the simulation results clearly reflect the initial transport of holes. The motion of hole concentration (blue) occurs in the predominantly center ZB region either towards ($\phi = 90^\circ$) or away from ($\phi = 270^\circ$) the first upper WZ segment at photoexcitation. These distinct starting

conditions lead either to an accumulation of holes near or in the region with the high stacking fault density or to their delocalization in the predominantly center ZB region (apart from hole trapping in WZ segments). The hole distributions in the ZB part of the NW are indicated by black dotted lines in figure 5(b) as a guide to the eye.

In the next step we move on to the product of the electron and hole distribution $n \cdot p$ in the center panels of figure 5(b). First, the modulation of the ZB exciton transition (blue transient) can be assigned to the charge carrier dynamics in the center ZB part of the NW. For $\phi = 90^\circ$ (parallel orientation), $n \cdot p$, exhibits two distinct maxima per SAW cycle in the ZB part which are marked by two black dashed ellipses in lower center panel. These maxima are located close to the interface between the center ZB part and the first upper WZ segment. As can be seen in the left lower panel of figure 5(b) these maxima arise from the recombination of the oscillating electrons in the center ZB region (orange) and the hole concentration (blue) which are accumulated with in the center ZB region near the first upper WZ segment. In our experimental data in figure 5(a), we can identify these recombination channels as two distinct peaks in the time-delayed emission signal, which are marked by black arrows. In contrast, for $\phi = 270^\circ$ (antiparallel orientation), our calculations show an extended domain of large $n \cdot p$ marked by the green dashed ellipse in the upper center panel. Here, the oscillating electrons remain within the delocalized hole concentration as they are accelerated away from the first upper WZ segment. Since $n \cdot p$ remains high over an extended time interval, the experimental data in figure 5(a) shows an extended, T_{SAW} -periodic plateau which is marked by the green arrow. Note, for the phases $\phi = 0^\circ$ and $\phi = 180^\circ$, the electric field is orientated perpendicular to the NW resulting in a reduced axial acceleration of holes in the ZB phase at photoexcitation. Hence, holes in the center ZB phase predominantly remain stationary at the point of generation for $\phi = 0^\circ$ or dissociate only partially from the point of generation for $\phi = 180^\circ$. Consequently, this results in a similar, yet not so efficiently transported hole distribution as obtained for the phase $\phi = 90^\circ$ and, thus again, in two recombination events per cycle which are also observed in our experimental data.

Second, the modulation of both indirect exciton transitions of **NW1** (red and green transients) is mostly governed by the charge carrier dynamics in the region with high stacking fault density which is modeled by the two upper WZ segments in our calculations. For both/all SAW phases, $n \cdot p$ (center panels) exhibits two distinct intensity maxima per SAW cycle which are located at lower and upper interface of each upper WZ segment, and which are marked by red and grey dashed ellipses in the lower and upper center panels. Both maxima result from the recombination of holes trapped at WZ segments and electrons, which are accelerated in the respective directions towards the defects. They are attributed to the two recombination events which are highlighted by red and grey arrows in the experimental data in figure 5(a). Note, the quenching of the intensity modulation of the indirect exciton transitions each period is assigned to the acceleration

of electrons towards the lower ZB part of the NW, thus, partially removing the electrons from the region with the stacking faults. Moreover, the emission intensity clearly depends on the orientation of electric field at the time of the laser excitation programming the electron concentration with in the WZ segments. For $\phi = 270^\circ$, electrons are initially injected into the region with in the WZ segments leading to an increased electron concentration within the region of stacking faults compared to the phase $\phi = 90^\circ$ (left panels in figure 5(b)). This gives rise to an increase of intensity maxima of $n \cdot p$ which are located at the upper interfaces of the WZ segments (marked by red dashed ellipses) resulting from the acceleration of electrons towards the lower ZB part of the NW. For $\phi = 270^\circ$, these intensity maxima are increased compared to the maxima of the following SAW cycle which are located at the lower interfaces (grey dashed ellipses), and which is clearly contrary to the case for $\phi = 90^\circ$. For $\phi = 90^\circ$, the intensity maxima at the upper interfaces are clearly reduced compared to maxima of the next SAW cycle located at the lower interfaces. This behavior is associated with the experimentally observed increase of the emission intensity at $t = 8.3\text{ns}$ for $\phi = 270^\circ$ (red arrows). Note, that $n \cdot p$ shows similar emission intensity at the lower twin segment for both phases which we assume to have a reduced impact on the modulation of both indirect exciton transitions of the **NW1**.

Next, we present analogous data from **NW2**. The measured transients of free ZB (blue), the indirect ZB/twin (green) and indirect twin/ZB/twin (orange) exciton transitions are depicted for $+k$ - propagating SAWs in figure 6(a). Again, all transitions of **NW2** show characteristic intensity modulations, which are—in strong contrast to **NW1**—almost identical for both propagation direction. The ZB transition exhibits two distinct recombination events per SAW period. The intensity of the first event of each cycle clearly exceeds the second event for all phases. Moreover, the temporal delay between both events oscillates as the phase is tuned, being maximum at $\phi = 90^\circ$ and minimal at $\phi = 270^\circ$. The ZB/twin transient exhibits two dominant recombination events (marked by grey and red arrows) per SAW cycle which are less pronounced compared to **NW1**. Moreover, the intensities of both events strongly depend on phase and only weakly on the SAW propagation direction. For $+k$ -propagating SAWs and $\phi = 90^\circ$, the second event (marked by red arrow) is slightly more pronounced event and persists over long timescales. In contrast, the intensity of this second event strongly reduces with each SAW period for $\phi = 270^\circ$. The indirect twin/ZB/twin (orange) exciton transition exhibits similar yet less pronounced intensity modulations as the ZB/twin exciton transition with both recombination events. Such a behavior may be attributed to the reduced oscillatory motion of electrons within the shorter ZB segments as well as to the reduced activation energy of electrons due to quantum confinement, or may also result from the increase of the density of short segments towards the upper end of the NW.

Again, the results of numerical calculations in figure 6(b) show that the key characteristics of intensity modulations can be understood by considering the initial distributions of holes

(blue) at the time of photoexcitation and the sinusoidal trajectories of the electrons (orange). For $+k$ -SAW propagation and all phases, holes are mostly localized inside the two twin segments with a higher concentration in the upper twin segment and in the ZB part between both segments. Electrons mainly oscillate *in between* the two twin segments where they are retained. This behavior is in strong contrast to the results on Type-1 NWs (NW1), for which a net directional transport of electrons is observed for the SAW propagating towards the ZB-region of the NW. For Type-2 NWs (NW2), the twin segment in the lower part of the NW forms a barrier and electrons are reflected from this interface. In combination with the reflection at the upper interface, the cyclic motion of electrons is mainly restricted to the center part and almost independent on the SAW propagation direction.

For $+k$ -propagating SAW, the propagation direction is orientated towards the upper twin segment. For $\phi = 90^\circ$, the initial transport of holes occurs towards this segment resulting in the accumulation of the hole concentration in the ZB region near the upper segment (lower left panel in figure 6(b)). Consequently, the electrons, oscillating in the ZB region between the two twin segments, can recombine with quasi-stationary holes two times per SAW cycle and $n \cdot p$ (lower center panel) exhibits two distinct maxima per SAW cycle in the ZB part between both twin segments which are marked by two black dashed ellipses in the lower center panel. This behavior is attributed to the observed intensity modulation of the ZB transient in the experimental data (marked by two black arrows in figure 6(a)). For $\phi = 270^\circ$, holes are delocalized between both twin defects (upper left panel in figure 6(b)) and our calculations show a continuous domain of large $n \cdot p$ with an increased initial intensity (marked by the green dashed ellipse in upper center panel). In our experimental data in figure 6(a), we can identify this recombination as temporally reduced reemergence of the intensity of the ZB transient (marked by a green arrow) showing also an increased initial intensity in the time-delayed emission signal.

Moreover, the two dominant recombination events of the experimentally observed indirect ZB/twin exciton transition can be assigned to recombination of electrons and holes occurring at both interfaces of each segment. At these interfaces, $n \cdot p$ (center panels) exhibits one distinct maximum per SAW cycle, marked by grey and red dashed ellipses. Obviously, the recombination event occurring at the defect located in SAW propagation direction is slightly more pronounced in our calculations of $n \cdot p$ compared to the corresponding second event of the same SAW cycle [marked by red dashed ellipse in figure 6(b)]. This behavior mainly results from the more efficient transport of electrons in the propagation direction of the SAW and may lead to the weak dependence of the SAW propagation direction on the experimentally observed indirect transients.

The data shown here are corroborated by analogous comprehensive experimental data and numerical modelling for $-k$ -propagating SAWs performed for both NWs. These are included in supplementary section 4 of the supporting material.

3. Discussion and conclusions

We conducted a comprehensive study on exemplary polytypic GaAs NWs employing TEM structural characterization and optical and AOE spectroscopy. In our TEM analysis and scanning PL spectroscopy we identify two families of NWs with different degrees of polytypism. The characteristic crystal phase mixing in these two polytypic NWs induce distinct type-II band edge modulations giving rise to three characteristic coupled recombination channels. The first Type-1 exhibits two different regions of the NW, a near pristine ZB region and a highly disordered region consisting of extended WZ and ZB segments. In contrast, the second Type-2 is pure ZB with the twin defect density slightly increasing along the NW. Consequently, both types of NWs differ in their recombination dynamics, yet show a triggered exchange between different channels within each NW. The different crystal structure results in the formation of distinct decay channels due to the type-II band edge modulation induced by crystal phase mixing. We select two representative NWs for detailed characterization using SAW-based optical spectroscopy. First, we show that the suppression of the optical emission intensity by the SAW exhibits markedly different behavior for the two types of NWs. The Type-1 NW shows clear non-monotonic quenching for spatially indirect transitions between ZB and WZ segments which depends on the propagation of the SAW. In contrast, the Type-2 NW shows almost perfect monotonic quenching independent on the SAW direction. These pronounced differences are clear fingerprints of the impact of the distinct crystal structure modulations in the two types of NWs on the acousto-electric charge transport. Second, we employ contact-free AOES to probe coupled charge carrier dynamics of different interconnected recombination channels in these two types of NWs with sub-nanosecond resolution. Because both types of NWs differ in their recombination dynamics, they show SAW-triggered carrier exchange between different channels within each NW. These result in characteristic intensity modulations which are observed in experiment. For the Type-1 NW, these modulations strongly depend on the SAW propagation direction and the studied recombination channel. In contrast, Type-2 NW shows almost identical modulations for both propagation directions and for each individual decay channel. Third, we corroborate our experimental findings by numerical calculations of the SAW-driven spatio-temporal carrier dynamics for two very general bandedge modulations of the two types of NWs. These calculations, which assume either two WZ segments and one twin segment or two twin segments at different positions along the NW axis, reproduce the most important features found in our experimental observations. This good qualitative agreement using realistic values of the electron and hole transport mobilities and barrier heights shows that our general model is able to reproduce the key physical processes underlying our experimental observations. For example, they nicely confirm efficient trapping of holes in WZ and twin segments, which leads to long-time persistent storage. Electrons, in contrast, show pronounced dynamics in ZB parts. Moreover, they show that carrier

transport is efficient inside the individual segments. For Type-1 NWs the presence of higher barriers in one direction leads to a net transport of electrons by a SAW propagating towards the part of low WZ or twin defect density. Consequently, the Type-1 NW shows a clear dependence of the intensity modulations on the SAW propagation direction due to net transport in one direction. For Type-2 NWs the presence of lower barriers at both ends of the NW results in an oscillatory motion and no directionality is observed in experiment.

In conclusion, we study coupled carrier dynamics in polytypic GaAs NWs in the limit of low carrier concentrations. The dynamics are driven by a ≈ 200 MHz piezoelectric SAW and detected on the underlying timescales with sub-nanosecond time resolution. We present direct evidence for interconnected recombination dynamics and carrier transport set by the distribution of WZ and twin defects within the NWs. The results clearly show that holes are efficiently trapped in WZ segments and that already a low degree of crystal phase mixing may result in an efficient suppression of electron transport at low temperatures. Thus, long range (coherent) electrical transport in NW at low carrier concentrations require near pristine NWs with vanishing crystal phase mixing. Our experimental data are compared to numerical simulation which assume a basic bandstructure modulation due to polytypism. Simulations reproduce the key features observed in experiment which demonstrates that the considered bandstructure modulation contains all relevant parameters. This shows, that detailed knowledge of the structural parameters on the nanoscale are not required to explain mesoscopic transport phenomena. Moreover, our approach can be extended to different material systems, NW-based heterostructures [61–63] or to study activation and capture processes in temperature dependent experiments [64].

Acknowledgments

This work was supported by the Deutsche Forschungsgemeinschaft (DFG) via the Research grants KR3790/6-1 and KO4005/6-1. We thank Achim Wixforth and Ferdinand Haider for enduring support and invaluable discussions.

Data availability statement

The data that support the findings of this study are available upon reasonable request from the authors.

ORCID iDs

Maximilian M Sonner  <https://orcid.org/0000-0002-6095-4610>

Gregor Koblmüller  <https://orcid.org/0000-0002-7228-0158>

Hubert J Krenner  <https://orcid.org/0000-0002-0696-456X>

References

- [1] Appenzeller J, Knoch J, Bjork M T, Riel H, Schmid H and Riess W 2008 Toward nanowire electronics *IEEE Trans. Electron Devices* **55** 2827
- [2] Chen R, Tran T-T D, Ng K W, Ko W S, Chuang L C, Sedgwick F G and Chang-Hasnain C 2011 Nanolasers grown on silicon *Nat. Photon.* **5** 170
- [3] Mayer B *et al* 2013 Lasing from individual GaAs-AlGaAs core-shell nanowires up to room temperature *Nat. Commun.* **4** 2931
- [4] Yao M, Huang N, Cong S, Chi C-Y, Seyedi M A, Lin Y-T, Cao Y, Povinelli M L, Dapkus P D and Zhou C 2014 GaAs nanowire array solar cells with axial p-i-n junctions *Nano Lett.* **14** 3293
- [5] Tomioka K, Yoshimura M and Fukui T 2012 A III-V nanowire channel on silicon for high-performance vertical transistors *Nature* **488** 189
- [6] Koguchi M, Kakibayashi H, Yazawa M, Hiruma K and Katsuyama T 1992 Crystal structure change of GaAs and InAs whiskers from zinc-blende to wurtzite type *Japan. J. Appl. Phys.* **31** 2061
- [7] Hiruma K, Yazawa M, Haraguchi K, Ogawa K, Katsuyama T, Koguchi M and Kakibayashi H 1993 GaAs free-standing quantum-size wires *J. Appl. Phys.* **74** 3162
- [8] Ohlsson B J, Björk M T, Magnusson M H, Deppert K, Samuelson L and Wallenberg L R 2001 Size-, shape-, and position-controlled GaAs nano-whiskers *Appl. Phys. Lett.* **79** 3335
- [9] Caroff P, Dick K A, Johansson J, Messing M E, Deppert K and Samuelson L 2009 Controlled polytypic and twin-plane superlattices in III-V nanowires *Nat. Nanotechnol.* **4** 50
- [10] Joyce H J, Wong-Leung J, Gao Q, Hoe Tan H and Jagadish C 2010 Phase perfection in zinc blende and wurtzite III-V nanowires using basic growth parameters *Nano Lett.* **10** 908
- [11] Vainorius N, Jacobsson D, Lehmann S, Gustafsson A, Dick K A, Samuelson L and Pistol M-E 2014 Observation of Type-II recombination in single wurtzite/zinc-blende GaAs heterojunction nanowires *Phys. Rev. B* **89** 165423
- [12] Mattila M, Hakkarainen T, Mulot M and Lipsanen H 2006 Crystal-structure-dependent photoluminescence from InP nanowires *Nanotechnology* **17** 1580
- [13] Bao J, Bell D C, Capasso F, Wagner J B, Mårtensson T, Trägårdh J and Samuelson L 2008 Optical properties of rotationally twinned InP nanowire heterostructures *Nano Lett.* **8** 836
- [14] Spirkoska D *et al* 2009 Structural and optical properties of high quality zinc-blende/wurtzite GaAs nanowire heterostructures *Phys. Rev. B* **80** 245325
- [15] Akopian N, Patriarche G, Liu L, Harmand J-C and Zwiller V 2010 Crystal phase quantum dots *Nano Lett.* **10** 1198
- [16] Heiss M *et al* 2011 Direct correlation of crystal structure and optical properties in wurtzite/zinc-blende GaAs nanowire heterostructures *Phys. Rev. B* **83** 045303
- [17] Jahn U, Lähnemann J, Pfüller C, Brandt O, Breuer S, Jenichen B, Ramsteiner M, Geelhaar L and Riechert H 2012 Luminescence of GaAs nanowires consisting of wurtzite and zinc-blende segments *Phys. Rev. B* **85** 045323
- [18] Graham A M, Corfdir P, Heiss M, Conesa-Boj S, Uccelli E, Fontcuberta i Morral A and Phillips R T 2013 Exciton localization mechanisms in wurtzite/zinc-blende GaAs nanowires *Phys. Rev. B* **87** 125304
- [19] Senichev A V, Talalaev V G, Shtrom I V, Blumtritt H, Cirlin G E, Schilling J, Lienau C and Werner P 2014 Nanospectroscopic imaging of twinning superlattices in an individual GaAs-AlGaAs core-shell nanowire *ACS Photonics* **1** 1099

- [20] Rudolph D, Schweickert L, Morkötter S, Hanschke L, Hertenberger S, Bichler M, Koblmüller G, Abstreiter G and Finley J J 2013 Probing the trapping and thermal activation dynamics of excitons at single twin defects in GaAs–AlGaAs core–shell nanowires *New J. Phys.* **15** 113032
- [21] Schroer M D and Petta J R 2010 Correlating the nanostructure and electronic properties of InAs nanowires *Nano Lett.* **10** 1618
- [22] Thelander C, Caroff P, Plissard S, Dey A W and Dick K A 2011 Effects of crystal phase mixing on the electrical properties of InAs nanowires *Nano Lett.* **11** 2424
- [23] Morkötter S *et al* 2015 Demonstration of confined electron gas and steep-slope behavior in delta-doped GaAs–AlGaAs core–shell nanowire transistors *Nano Lett.* **15** 3295
- [24] Kinzel J B *et al* 2016 The native material limit of electron and hole mobilities in semiconductor nanowires *ACS Nano* **10** 4942
- [25] Delsing P *et al* 2019 The 2019 surface acoustic waves roadmap *J. Phys. D: Appl. Phys.* **52** 353001
- [26] Rayleigh L 1885 On waves propagated along the plane surface of an elastic solid *Proc. London Math. Soc.* **s1–17** 4
- [27] Sonner M M, Khosravi F, Janker L, Rudolph D, Koblmüller G, Jacob Z and Krenner H J 2021 Ultrafast electron cycloids driven by the transverse spin of a surface acoustic wave *Sci. Adv.* **7** eabf7414
- [28] Sader E, Harnik E and Kovnovich S 1980 Acoustoelectric measurement of electron mobility and diffusion in ultrathin evaporated gold films *Appl. Phys. Lett.* **36** 430
- [29] Adler R, Janes D, Hunsinger B J and Datta S 1981 Acoustoelectric measurement of low carrier mobilities in highly resistive films *Appl. Phys. Lett.* **38** 102
- [30] Wixforth A, Scriba J, Wassermeier M, Kotthaus J P, Weimann G and Schlapp W 1988 Interaction of surface acoustic waves with a two-dimensional electron system in a LiNbO₃–GaAs/AlGaAs sandwich structure *J. Appl. Phys.* **64** 2213
- [31] Streibl M, Wixforth A, Kotthaus J P, Govorov A O, Kadow C and Gossard A C 1999 Imaging of acoustic charge transport in semiconductor heterostructures by surface acoustic waves *Appl. Phys. Lett.* **75** 4139
- [32] Fuhrmann D A, Krenner H J, Wixforth A, Curran A, Prior K A, Warburton R J and Ebbecke J 2010 Noninvasive probing of persistent conductivity in high quality ZnCdSe/ZnSe quantum wells using surface acoustic waves *J. Appl. Phys.* **107** 093717
- [33] Poole T, Bandhu L and Nash G R 2015 Acoustoelectric photoresponse in graphene *Appl. Phys. Lett.* **106** 133107
- [34] Preciado E *et al* 2015 Scalable fabrication of a hybrid field-effect and acousto-electric device by direct growth of monolayer MoS₂/LiNbO₃ *Nat. Commun.* **6** 8593
- [35] Roche C, Zimmermann S, Wixforth A, Kotthaus J P, Böhm G and Weimann G 1997 Acoustically driven storage of light in a quantum well *Phys. Rev. Lett.* **78** 4099
- [36] Santos P V, Ramsteiner M and Jungnickel F 1998 Spatially resolved photoluminescence in GaAs surface acoustic wave structures *Appl. Phys. Lett.* **72** 2099
- [37] García-Cristóbal A, Cantarero A, Alsina F and Santos P V 2004 Spatiotemporal carrier dynamics in quantum wells under surface acoustic waves *Phys. Rev. B* **69** 205301
- [38] Schüle F J R, Pustiowski J, Müller K, Bichler M, Koblmüller G, Finley J J, Wixforth A and Krenner H J 2012 Surface acoustic wave controlled charge dynamics in a thin InGaAs quantum well *JETP Lett.* **95** 575
- [39] Schüle F J R, Müller K, Bichler M, Koblmüller G, Finley J J, Wixforth A and Krenner H J 2013 Acoustically regulated carrier injection into a single optically active quantum dot *Phys. Rev. B* **88** 085307
- [40] Janker L, Tong Y, Polavarapu L, Feldmann J, Urban A S and Krenner H J 2019 Real-time electron and hole transport dynamics in halide perovskite nanowires *Nano Lett.* **19** 8701
- [41] Alsina F, Santos P V, Schönherr H-P, Seidel W, Ploog K H and Nötzel R 2002 Surface-acoustic-wave-induced carrier transport in quantum wires *Phys. Rev. B* **66** 165330
- [42] Alsina F, Santos P V, Hey R, García-Cristóbal A and Cantarero A 2001 Dynamic carrier distribution in quantum wells modulated by surface acoustic waves *Phys. Rev. B* **64** 041304
- [43] Richter A, Behme G, Süptitz M, Lienau C, Elsaesser T, Ramsteiner M, Nötzel R and Ploog K H 1997 Real-space transfer and trapping of carriers into single GaAs quantum wires studied by near-field optical spectroscopy *Phys. Rev. Lett.* **79** 2145
- [44] Gell J R, Ward M B, Young R J, Stevenson R M, Atkinson P, Anderson D, Jones G A C, Ritchie D A and Shields A J 2008 Modulation of single quantum dot energy levels by a surface-acoustic-wave *Appl. Phys. Lett.* **93** 081115
- [45] Weiß M *et al* 2014 Dynamic acoustic control of individual optically active quantum dot-like emission centers in heterostructure nanowires *Nano Lett.* **14** 2256
- [46] Kinzel J B, Rudolph D, Bichler M, Abstreiter G, Finley J J, Koblmüller G, Wixforth A and Krenner H J 2011 Directional and dynamic modulation of the optical emission of an individual GaAs nanowire using surface acoustic waves *Nano Lett.* **11** 1512
- [47] Büyükköse S, Hernández-Minguez A, Vratzov B, Somaschini C, Geelhaar L, Riechert H, van der Wiel W G and Santos P V 2014 High-frequency acoustic charge transport in GaAs nanowires *Nanotechnology* **25** 135204
- [48] Hernández-Minguez A *et al* 2012 Acoustically driven photon antibunching in nanowires *Nano Lett.* **12** 252
- [49] Rudolph D *et al* 2013 Spontaneous alloy composition ordering in GaAs–AlGaAs core–shell nanowires *Nano Lett.* **13** 1522
- [50] Rudolph D, Schweickert L, Morkötter S, Loitsch B, Hertenberger S, Becker J, Bichler M, Abstreiter G, Finley J J and Koblmüller G 2014 Effect of interwire separation on growth kinetics and properties of site-selective GaAs nanowires *Appl. Phys. Lett.* **105** 033111
- [51] Demichel O, Heiss M, Bleuse J, Mariette H and Fontcuberta i Morral A 2010 Impact of surfaces on the optical properties of GaAs nanowires *Appl. Phys. Lett.* **97** 201907
- [52] Erhard N *et al* 2015 Ultrafast photodetection in the quantum wells of single AlGaAs/GaAs-based nanowires *Nano Lett.* **15** 6869
- [53] Algra R E, Verheijen M A, Borgström M T, Feiner L-F, Immink G, van Enckevort W J P, Vlieg E and Bakkers E P A M 2008 Twinning superlattices in indium phosphide nanowires *Nature* **456** 369
- [54] Senichev A, Corfdir P, Brandt O, Ramsteiner M, Breuer S, Schilling J, Geelhaar L and Werner P 2018 Electronic properties of wurtzite GaAs: a correlated structural, optical, and theoretical analysis of the same polytypic GaAs nanowire *Nano Res.* **11** 4708
- [55] Loitsch B, Müller M, Winnerl J, Veit P, Rudolph D, Abstreiter G, Finley J J, Bertram F, Christen J and Koblmüller G 2016 Microscopic nature of crystal phase quantum dots in ultrathin GaAs nanowires by nanoscale luminescence characterization *New J. Phys.* **18** 1
- [56] Fuhrmann D A, Thon S M, Kim H, Bouwmeester D, Petroff P M, Wixforth A and Krenner H J 2011 Dynamic modulation of photonic crystal nanocavities using gigahertz acoustic phonons *Nat. Photon.* **5** 605
- [57] Völk S, Knall F, Schüle F J R, Truong T A, Kim H, Petroff P M, Wixforth A and Krenner H J 2011 Direct observation of dynamic surface acoustic wave controlled carrier injection into single quantum posts using phase-resolved optical spectroscopy *Appl. Phys. Lett.* **98** 023109
- [58] Sonner M M, Rudolph D, Koblmüller G and Krenner H J 2021 High-dimensional acousto-optoelectric correlation spectroscopy reveals coupled carrier dynamics in polytypic nanowires *Phys. Rev. Appl.* **16** 034010

- [59] Völk S, Schülein F J R, Knall F, Reuter D, Wieck A D, Truong T A, Kim H, Petroff P M, Wixforth A and Krenner H J 2010 Enhanced sequential carrier capture into individual quantum dots and quantum posts controlled by surface acoustic waves *Nano Lett.* **10** 3399
- [60] Völk S, Knall F, Schülein F J R, Truong T A, Kim H, Petroff P M, Wixforth A and Krenner H J 2012 Surface acoustic wave mediated carrier injection into individual quantum post nano emitters *Nanotechnology* **23** 285201
- [61] Fontcuberta A, Morral I, Spirkoska D, Arbiol J, Heigoldt M, Morante J R and Abstreiter G 2008 Prismatic quantum heterostructures synthesized on molecular-beam epitaxy GaAs nanowires *Small* **4** 899
- [62] Fickenscher M *et al* 2013 Optical, structural, and numerical investigations of GaAs/AlGaAs core-multishell nanowire quantum well tubes *Nano Lett.* **13** 1016
- [63] Sonner M M *et al* 2019 Breakdown of corner states and carrier localization by monolayer fluctuations in radial nanowire quantum wells *Nano Lett.* **19** 3336
- [64] Shi T, Jackson H E, Smith L M, Jiang N, Tan H H and Jagadish C 2016 Thermal delocalization of excitons in GaAs/AlGaAs quantum well tube nanowires *Nano Lett.* **16** 1392